JPE 18-6-10

https://doi.org/10.6113/JPE.2018.18.6.1708
ISSN(Print): 1598-2092 / ISSN(Online): 2093-4718

A Robust Dynamic Decoupling Control Scheme for PMSM Current Loops Based on Improved Sliding Mode Observer

Hanlin Shen*, Xin Luo*, Guilin Liang†, and Anwen Shen*

†,*School of Automation, Huazhong University of Science and Technology, Wuhan, China

Abstract

A complete current loop decoupling control strategy based on a sliding mode observer (SMO) is proposed to eliminate the influence of current dynamic coupling and back electromotive force (EMF) in the vector control of permanent magnet synchronous motors. With this strategy, current dynamic decoupling and back EMF compensation can be simultaneously achieved. Unlike conventional methods, the proposed strategy can avoid the disturbances caused by the parametric variations of motor systems and maintain the advantages of proportional integral (PI) controllers, which are robust and easy to operate. An improved SMO, which uses a special PI regulator other than a linear saturation function as the equivalent control law in the boundary layer of a sliding surface, is proposed to eliminate the estimated errors caused by the quasi-sliding mode and obtain a satisfactory decoupling performance. The stability and parameter robustness of the proposed strategy are also analyzed. Physical experimental results are presented to verify the validity of the method.

Key words: Back electromotive force, Decoupling, Permanent magnet synchronous motor (PMSM), Quasi-sliding mode, Sliding mode observer

I. INTRODUCTION

Permanent magnet synchronous motors (PMSMs) have been widely used in various industrial automation applications [1]-[4] due to their high efficiency, large output torque, reliability, small size, and other advantages. However, obtaining a high-performance PMSM drive control system is difficult due to the high order, strong coupling, and non-linear characteristics of PMSMs. The rotor field-oriented control is a usual control scheme. High performance can be achieved by ensuring that the drive control system has the proper current loop dynamic response. The stator current of a PMSM can be decomposed into flux and torque components through coordinate transformation, which allows a high dynamic response to be obtained by controlling the motor flux and torque, respectively. However, two main factors affect the current control loop [5]-[7]. The first factor is the current dynamic coupling. The vector control of $i_d = 0$ can only statically realize current decoupling. As motor speed increases, the dynamic coupled component between the d-axis and q-axis also increases. This condition means that a change in one of the current components leads to a change in the other components, eventually worsening the dynamic response of the current loop. The second factor is the back EMF. When the motor speed slowly changes, the variation of the EMF can be ignored. However, with sharp changes in motor speed, the back EMF of the motor abruptly changes, thereby increasing the adjustment difficulty of the current loop controller and reducing the current loop dynamic response.

Extensive research has been conducted to solve these problems. The available methods can be divided into two categories according to the different degrees of dependence on motor mathematical models. The first category comprises methods that depend solely on motor mathematical models [8]-[12], and these methods include the feedback decoupling method [8] and feedforward decoupling method [9]. These methods are simple and easy to implement, and they compensate for the theoretical value of the coupling term in the current controller output. However, these methods cannot

Manuscript received Feb. 4, 2018; accepted Jun. 21, 2018
Recommended for publication by Associate Editor Zheng Wang.
†Corresponding Author: liangguilin0228@163.com
Tel: +86-027-8754-1547, Fax: +86-027-8754-1547, Huazhong Univ. of Science and Tech.
*School of Automation, Huazhong Univ. of Science and Tech., China

realize current decoupling and back EMF compensation simultaneously, and they heavily depend on reliable motor parameters, such as resistance, inductance, and flux. With the motor running, the parametric variations worsen system performance [5].

The second category comprises the methods with low dependence on motor mathematical models [13]-[33], and they include error compensation decoupling and internal model decoupling. For the error compensation method in [13], two additional proportional integral (PI) controllers were used to provide signals for motors' *d*-axis and *q*-axis cross-coupling voltage compensation. In the case of parameter mismatch, the method with error compensation is more robust than the feedforward decoupling controller is, as revealed by two appropriate PI regulators in [14]. For the internal model decoupling in [15], the internal model control method was utilized to construct a robust decoupling current controller. The new controller is an extension of the traditional PI regulator, which comprises only one controller parameter. Although the two methods are better than feedforward decoupling in terms of the robustness of the parametric variations, they require additional techniques to compensate for the back EMF; furthermore, internal model decoupling is less effective than the error compensation method is in terms of stability [9].

Some methods have also been developed on the basis of the models in [18]-[21]. These methods combine the first category methods with the online parameter identification algorithm to adjust control parameters in real time. For example, the current controller in [18] is a combination of a PI regulator and feedback decoupling network; this combination helps minimize the interactions between the *d*-axis and the *q*-axis and eliminates the remaining interactions through an online adaptive cancellation. This method can reduce the sensitivity of the current controller to the parameters, but the online parameter identification makes the system increasingly complicated. Other studies [22]-[24] used intelligent control algorithms to reduce the dependence on motor mathematical models. Sliding mode control has also been introduced to realize current decoupling and back EMF compensation. In [25], a robust decoupling mechanism, including an adaptive flux observer and a sliding mode current estimator, was investigated to decouple the complicated flux and torque dynamics of an induction motor, and a total sliding mode control scheme was constructed without the reaching phase in conventional sliding mode control to enhance system robustness. However, this method depends on voltage signals and requires additional voltage sensors. In [26], [27], a new approach for current control that uses integral sliding mode (ISM) controllers was proposed to achieve decoupling. Synchronous frame control voltages are synthesized as the sum of the following two controller outputs: a traditional one (PI) that acts on an ideal plant model and an ISM controller. However, the control law of the ISM involves discontinuous sign functions, which will bring chattering to the current loop. In [28]-[31], a sliding mode observer (SMO) was used to estimate system uncertainties, including electrical and mechanical parameter variations, external disturbances, and unmodeled dynamics in practical applications. In [28], [29], a current controller was used as a sliding mode controller and combined with an SMO to realize current decoupling. This method depends on the current instruction value and involves discontinuous sign functions, which will bring chattering to the system. In [30], an internal model control was combined with an SMO as the current controller; the control law was a linear saturation function. In [31], an SMO was combined with generalized predictive control to satisfy the required control current loop of the motor. The application of the methods in [28]-[31] to actual systems is extremely complicated. In [32], a weighted integral-type sliding mode control algorithm was used to solve the chattering problem and obtain a fast response, but the selection of weight coefficients depends on experience. In [33], a method combining adaptive fast terminal sliding mode control and current feedforward control methods was proposed to solve the problems of the d-q current cross-coupling. However, this method is strict with regard to parameter selection to avoid convergence issues, and the control law involves exponential functions that require several arithmetical operations.

By summarizing the available literature, we propose a novel method on the basis of an SMO to obtain a complete current loop decoupling control and thereby solve the aforementioned problems. The proposed strategy can achieve current dynamic decoupling and back EMF compensation simultaneously. Compared with similar schemes, the proposed strategy can avoid the disturbances caused by the motor system's parametric variations and maintain the advantages of PI controllers, which are robust and easy to use. An improved SMO is proposed to obtain superior decoupling performance and eliminate the estimated errors caused by the quasi-sliding mode. This SMO uses a special PI regulator other than a linear saturation function as the equivalent control law in the boundary layer of the sliding surface. In the study, the stability and parameter robustness of the proposed strategy are also analyzed. The experimental results demonstrate that current dynamic decoupling and back EMF compensation can be accurately obtained with the proposed current loop decoupling control strategy.

This paper is organized as follows. In Section II, the mathematical model of a PMSM is introduced, and the influence of current coupling and back EMF is analyzed. In Section III, a traditional SMO is derived (part A), and its disadvantages are analyzed (part B). One such disadvantage is the sliding mode being unable to converge to the sliding surface, thereby leading to steady-state errors in the

compensation results. An improved SMO is then proposed (part C), and its stability is proven. In Section IV, the parameter robustness is analyzed. In Section V, the improved SMO method is verified by experiments. Finally, in Section VI, relevant conclusions are drawn.

II. Mathematical Model of PMSM

The PMSM model in a synchronous reference frame (d, q) is shown as follows:

$$\begin{cases} pi_d = \dfrac{u_d}{L_d} - \dfrac{R}{L_d} i_d + \dfrac{\omega_e L_q i_q}{L_d} \\ pi_q = \dfrac{u_q}{L_q} - \dfrac{R}{L_q} i_q - \dfrac{\omega_e L_d i_d}{L_q} - \dfrac{\omega_e \psi_f}{L_q} \end{cases} \tag{1}$$

where u_d, u_q; i_d, i_q; and L_d, L_q are the stator voltage, current, and inductance in the $d(q)$-axis of the PMSM, respectively. ω_e, R, ψ_f, and p are the electrical angular speed of the rotor, stator resistance, permanent magnet flux linkage, and differential operator, respectively. In Eq. (1), the term of the back EMF is $-\omega_e\psi_f$, and the current dynamic coupling terms between the d-axis and q-axis are $\omega_e L_q i_q$ and $-\omega_e L_d i_d$, respectively. The vector control of $i_d = 0$ statically realizes current decoupling by ignoring the terms of the back EMF and current dynamic coupling.

Fig. 1 shows the current control loop of the PMSM, in which the current controller is a PI regulator, T_d is the system delay time, and the part in the dotted box is the PMSM mathematical model. Given that the current dynamic coupling terms and back EMF are related to motor speed, the influence of coupling can be ignored when the motor speed is low. However, when the motor speed increases, the coupling worsens the system performance. For the back EMF, if the motor speed sharply changes, then the back EMF will abruptly change, ultimately increase the adjustment difficulty of the current loop PI controller, and reduce the current loop dynamic response. Employing several methods is important to realize current decoupling and back EMF compensation. The coupling term in the $d(q)$-axis is defined as follows to simplify the discussion:

$$\begin{cases} e_d = \omega_e L_q i_q \\ e_q = -\omega_e L_d i_d - \omega_e \psi_f \end{cases} \tag{2}$$

where e_d is the coupling term of the d-axis current and e_q is the sum of the coupling term of the q-axis current and back EMF. According to Eq. (2), the mathematical model of the PMSM can be rewritten as follows:

$$\begin{cases} pi_d = \dfrac{u_d}{L_d} - \dfrac{R}{L_d} i_d + \dfrac{e_d}{L_d} \\ pi_q = \dfrac{u_q}{L_q} - \dfrac{R}{L_q} i_q + \dfrac{e_q}{L_q} \end{cases} \tag{3}$$

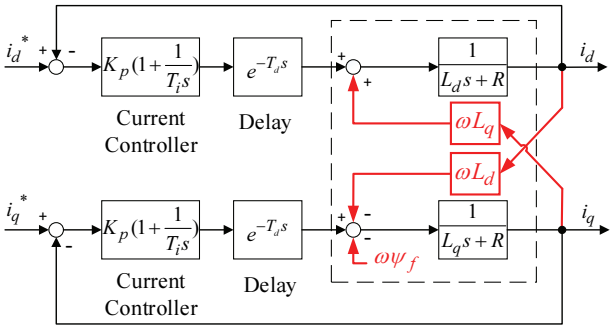

Fig. 1. Current control loop of PMSM.

III. Decoupling Method

Compensating for the coupling terms mentioned in Section II is necessary to ensure the high performance of the current loop. Therefore, a complete current loop decoupling control strategy based on an SMO is proposed. With this strategy, the current dynamic decoupling and back EMF can be compensated for simultaneously.

A. Mathematical Model of Sliding Mode Decoupling

According to sliding mode control theory [34], the SMO in the $d(q)$-axis is defined as follows:

$$\begin{cases} p\hat{I}_d = \dfrac{1}{L_d} u_d - \dfrac{R}{L_d} \hat{I}_d - \dfrac{k_d H(\sigma_d)}{L_d} \\ p\hat{I}_q = \dfrac{1}{L_q} u_q - \dfrac{R}{L_q} \hat{I}_q - \dfrac{k_q H(\sigma_q)}{L_q} \end{cases} \tag{4}$$

$$\begin{cases} \sigma_d = \bar{i}_d = \hat{I}_d - i_d \\ \sigma_q = \bar{i}_q = \hat{I}_q - i_q \end{cases} \tag{5}$$

where σ_d, σ_q are the sliding surface functions in the $d(q)$-axis; the definitions are shown in Eq. (5). $H(\sigma)$ is the equivalent control law. k_d, k_q and $\hat{I}_d$, $\hat{I}_q$ are the gains and current observations of the SMO, respectively. The error equation is obtained by subtracting Eq. (3) from Eq. (4) as follows:

$$\begin{cases} \dot{\sigma}_d = -\dfrac{R}{L_d}\sigma_d - \dfrac{k_d H(\sigma_d)}{L_d} - \dfrac{e_d}{L_d} \\ \dot{\sigma}_q = -\dfrac{R}{L_q}\sigma_q - \dfrac{k_q H(\sigma_q)}{L_q} - \dfrac{e_q}{L_q} \end{cases} \tag{6}$$

where $\dot{\sigma}$ is the derivative of the sliding surface function. Once the system moves to the sliding surface, the terms $\dot{\sigma}_d$, $\dot{\sigma}_q$, σ_d, and σ_q in Eq. (6) are evidently equal to zero, and the coupled EMF can then be obtained as Eq. (7).

$$\begin{cases} e_d = -k_d H(\sigma_d) \\ e_q = -k_q H(\sigma_q) \end{cases} \tag{7}$$

Eq. (8) must be satisfied to guarantee the stability of the aforementioned SMO [34]. Eq. (8) can also be rewritten as Eq. (9).

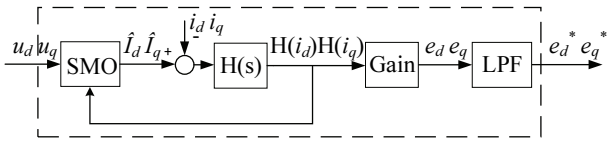

Fig. 2. Block diagram of the proposed control strategy.

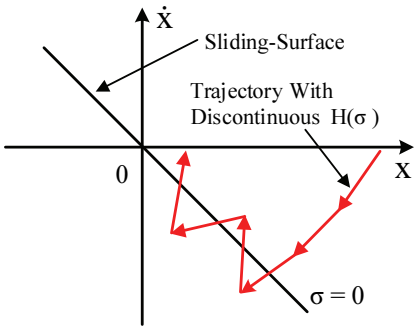

Fig. 3. Sliding mode trajectory with discontinuous H(σ).

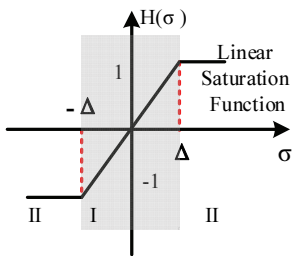

Fig. 4. Commonly selected equivalent control law $H(\sigma)$.

$$\lim_{s\to 0^+} \dot{\sigma} < 0 \ , \ \lim_{s\to 0^-} \dot{\sigma} > 0 \tag{8}$$

$$\sigma\dot{\sigma} \le 0 \tag{9}$$

Fig. 2 is the block diagram of the proposed decoupling strategy based on an SMO. The current dynamic decoupling and back EMF compensation are realized by substituting the estimated values of e_d, e_q into the current controller output. A first-order low-pass filter (LPF) is commonly used in SMOs to improve the results degraded by the discontinuous control law. Eq. (7) will then be changed to Eq. (10).

$$\begin{cases} e_d^* = -\dfrac{\omega_c}{s+\omega_c} k_d H(\sigma_d) \\ e_q^* = -\dfrac{\omega_c}{s+\omega_c} k_q H(\sigma_q) \end{cases} \tag{10}$$

where ω_c is the cut-off frequency of the LPF and e_d^*, e_q^* are the filter outputs of the coupled EMFs e_d, e_q.

The equivalent control law H(σ) is a discontinuous function in traditional sliding modes. Owing to the time delay and space lag in an actual system, the sliding mode is always accompanied by chattering, as indicated by the red trajectory in Fig. 3. Finding a way to weaken the inherent chattering is important in sliding mode control, and the most common method is to replace H(σ) with a continuous function. Fig. 4

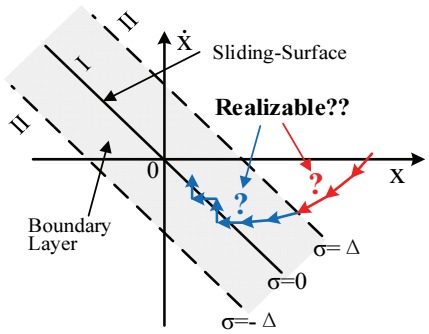

Fig. 5. Quasi-sliding mode trajectory.

is a linear saturation function that is usually selected as the equivalent control law [11]. The shadow region between [−Δ, Δ] is marked as region I, and the other region in Fig. 4 is marked as region II. As shown in Eq. (11), H(σ) is a proportional function in region I.

$$H(\sigma) = \begin{cases} 1 & \sigma > \Delta \\ \dfrac{\sigma}{\Delta} & |\sigma| < \Delta \\ -1 & \sigma < -\Delta \end{cases} \tag{11}$$

B. Convergence of Quasi-sliding Mode

When H(σ) is selected as Eq. (11), the sliding mode is changed as the quasi-sliding mode, which is divided into two parts by H(σ): regions I and II. Region I is a linear feedback control system, which is called the boundary layer of the sliding surface; the width of the boundary layer is denoted by Δ. Region II is a switch control system outside the boundary layer. The quasi-sliding mode must converge to the sliding surface. The expected convergent trajectory is shown in Fig. 5. The blue and red trajectories are the expected convergent trajectories in regions I and II, respectively. Owing to the addition of region I, the control system is considerably changed, and the convergences of the system in the two regions must be analyzed and deduced again.

As shown in Fig. 5, the convergence of region II should be discussed. Take the *d*-axis in Eq. (6) as an example. Two new sliding mode functions are defined, as shown in Eq. (12).

$$\hat{\sigma}_{d1} = \sigma_d - \Delta \ , \ \hat{\sigma}_{d2} = \sigma_d + \Delta \tag{12}$$

where $\hat{\sigma}_{d1}$ and $\hat{\sigma}_{d2}$ are the upper and lower boundaries of the boundary layer, respectively; the width of the boundary layer Δ is constant. Therefore, Eq. (13) can be obtained as follows:

$$\begin{cases} \dot{\hat{\sigma}}_{d1} = \dot{\sigma}_d - \dot{\Delta} = \dot{\sigma}_d \\ \dot{\hat{\sigma}}_{d2} = \dot{\sigma}_d + \dot{\Delta} = \dot{\sigma}_d \end{cases} \tag{13}$$

By substituting Eq. (6) into Eq. (13), we replace H(σ_d) with 1 and −1 in region II.

$$\begin{cases} L_d \dot{\hat{\sigma}}_{d1} = -R\sigma_d - k_d - e_d \\ L_d \dot{\hat{\sigma}}_{d2} = -R\sigma_d + k_d - e_d \end{cases} \tag{14}$$

According to Eq. (8), the sufficient condition to keep the boundary layer reachable is described in Eq. (15).

$$\lim_{\hat{\sigma}_{d1}\to 0^+}\dot{\hat{\sigma}}_{d1}<0\ ,\ \lim_{\hat{\sigma}_{d2}\to 0^-}\dot{\hat{\sigma}}_{d2}>0 \tag{15}$$

As defined in Eq. (12), $\hat{\sigma}_{d1}\to 0^+$ is equivalent to $\sigma_d\to\Delta^+$. If $\sigma_d\to\Delta^+$ is substituted into the first equation in Eq. (14), then $\dot{\hat{\sigma}}_{d1}<0$ will be true when Eq. (16) is satisfied. Similarly, $\hat{\sigma}_{d2}\to 0^-$ is equivalent to $\sigma_d\to-\Delta^-$. If $\sigma_d\to-\Delta^-$ is substituted into the second equation in Eq. (14), then $\dot{\hat{\sigma}}_{d2}>0$ will also be true when Eq. (16) is satisfied. Thus, Eq. (15) will be established when Eq. (16) is satisfied, and the boundary layer in the $d(q)$-axis is reachable in region II. That is, the red convergent trajectory in Fig. 5 can be achieved under certain conditions.

$$k_d\geq|e_d|,k_q\geq|e_q| \tag{16}$$

Given that the red convergent trajectory is achievable, if the blue convergent trajectory in region I is also performed, then the proposed decoupling control strategy will be realized. Fig. 6 shows the closed loop of the linear feedback system in region I. $\hat{e}_{d(q)}$ is the observed result of the $d(q)$-axis coupled EMF $e_{d(q)}$. $E(s)$ is the error's Laplace transform between the current observed result and the system feedback value. The delay is evident in the closed loop due to the iteration in the algorithm implementation. T_s is the cycle time of the current loop control.

According to Fig. 6, the transfer function from $\hat{e}_{d(q)}$ to $e_{d(q)}$ can be obtained as follows:

$$\frac{\hat{e}_{d(q)}(\mathrm{s})}{e_{d(q)}(\mathrm{s})}=\frac{k_{d(q)}}{\Delta T_sL_{d(q)}s^2+\Delta(T_sR+L_{d(q)})s+(\Delta R+k_{d(q)})} \tag{17}$$

According to the closed-loop characteristic equation of the system, we can easily obtain the Routh criterion list shown in Table I.

$k_{d(q)}$, T_s, and Δ are positive, along with the parameters in the first column of the Routh criterion list; therefore, the system is stable. After discussing the stability of the system, we can then deduce the current error equation as follows:

$$E(\mathrm{s})=-\frac{(T_ss+1)(L_{d(q)}s+R)}{(L_{d(q)}s+R)(T_ss+1)+\dfrac{k_{d(q)}}{\Delta}}R(\mathrm{s}) \tag{18}$$

where $R(s)$ is the input function. When $R(s)$ is the unit step function, the system steady-state error can be obtained as Eq. (19).

$$e_{ss}=\lim_{s\to 0}sE(s)=\lim_{s\to 0}-\frac{(T_ss+1)(L_{d(q)}s+R)\mathrm{s}}{(L_{d(q)}s+R)(T_ss+1)+\dfrac{k_{d(q)}}{\Delta}}R(\mathrm{s})=-\frac{\Delta R}{\Delta R+k_{d(q)}} \tag{19}$$

The steady-state error e_{ss} is clearly not zero and is unrelated to the boundary layer width Δ. The width Δ cannot be extremely small; otherwise, the obtained chattering will be extremely large, and the performance of the system deteriorates. In such a case, the blue convergent trajectory in Fig. 5 is unattainable.

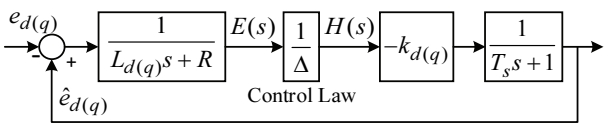

Fig. 6. Linear feedback system in region I.

TABLE I
ROUTH CRITERION LIST

	1st	2nd
s^2	$\Delta T_s L_{d(q)}$	$\Delta R+k_{d(q)}$
s^1	$\Delta(T_s R+ L_{d(q)})$	0
s^0	$\Delta R+k_{d(q)}$	0

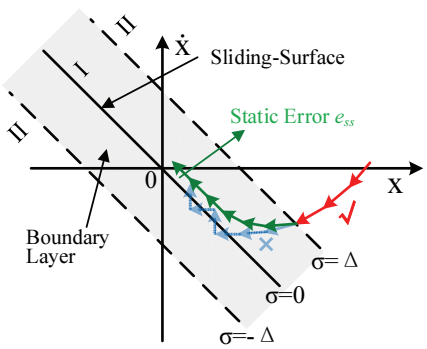

Fig. 7. Quasi-sliding mode trajectory.

The actual convergence of the quasi-sliding mode, as described previously, is illustrated in Fig. 7. The system can converge to the boundary layer of the sliding surface by choosing an appropriate $k_{d(q)}$. However, the blue convergent trajectory region I cannot be realized. The green trajectory shows the actual convergent trajectory in region I. A steady-state error e_{ss} exists between the observed current and the feedback current. As e_{ss} cannot be neglected, the system must eliminate it; otherwise, it will worsen the performance of the proposed decoupling control strategy.

C. Improved Quasi-sliding Mode Method

As discussed in part B, the quasi-sliding mode cannot converge to the sliding surface because the control law of the SMO is only a proportional element in region I. An integrating element is introduced to design a novel equivalent control law and eliminate steady-state errors e_{ss} effectively. The linear saturation function is replaced by a special PI regulator in Eq. (20), where $k_{pd(q)}$ and $k_{id(q)}$ are the proportional and integrating coefficients, respectively. The improved control law also has a boundary layer and is divided into two parts. Region II is the same as that in part B. Region I is still a linear feedback control system; however, unlike the

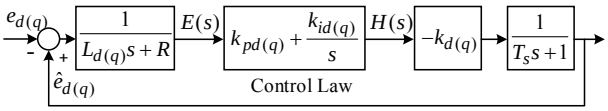

Fig. 8. Linear feedback system with special PI regulator in region I.

TABLE II
ROUTH CRITERION LIST

	1	2
s^3	$T_sL_{d(q)}$	$R+k_{d(q)}k_{pd(q)}$
s^2	$(T_s R+L_{d(q)})$	$k_{d(q)}k_{id(q)}$
s^1	C	0
s^0	$k_{d(q)}k_{id(q)}$	0

equivalent control law in Part B, the presented PI regulator is expected as mentioned above. Notably, when the system runs outside the boundary layer, the integral term is cleared. That is to say, each time the system moves into the boundary layer, the integral term is rebuilt.

$$H(\sigma)=\begin{cases}1 & \sigma>\Delta \\ 1 & \text{C1} \\ k_{pd(q)}\sigma+k_{id(q)}\int\sigma dt & \text{C2} \\ -1 & \text{C3} \\ -1 & \sigma<-\Delta\end{cases} \tag{20}$$

C1: $|\sigma|<\Delta, k_{pd(q)}\sigma+k_{id(q)}\int\sigma dt>1$

C2: $|\sigma|<\Delta, \left|k_{pd(q)}\sigma+k_{id(q)}\int\sigma dt\right|\le 1$

C3: $|\sigma|<\Delta, k_{pd(q)}\sigma+k_{id(q)}\int\sigma dt<-1$

The convergence in region II is the same as that analyzed above. The boundary layer becomes reachable when Eq. (16) is satisfied. For region I, the analysis procedure is similar to that in Part B. Fig. 8 shows the block diagram of the system with the special PI regulator in region I.

According to Fig. 8, the transfer function from $\hat{e}_{d(q)}$ to $e_{d(q)}$ of the linear feedback system with the special PI regulator can be obtained as Eq. (21).

$$\frac{\hat{e}_{d(q)}(s)}{e_{d(q)}(s)}=\frac{A_1 s+A_2}{T_sL_{d(q)}s^3+(T_sR+L_{d(q)})s^2+(R+A_1)s+A_2} \tag{21}$$
$$A_1=k_{d(q)}k_{pd(q)}, A2=k_{d(q)}k_{id(q)}$$

$$c=\frac{k_{d(q)}k_{id(q)}T_sL_{d(q)}-T_sR^2-L_{d(q)}R}{-(T_sR+L_{d(q)})}+\frac{-k_{d(q)}k_{pd(q)}T_sR-k_{d(q)}k_{pd(q)}L_{d(q)}}{-(T_sR+L_{d(q)})} \tag{22}$$

The Routh criterion list according to the closed-loop characteristic equation of the system in Eq. (21) is shown in Table II.

c in Table II is obtained with Eq. (22). The parameters in the first column of the Routh criterion list must be positive to maintain system stability. Given that $k_{pd(q)}$, $k_{id(q)}$ are positive, c is positive, and the system is stable when Eq. (23) is satisfied.

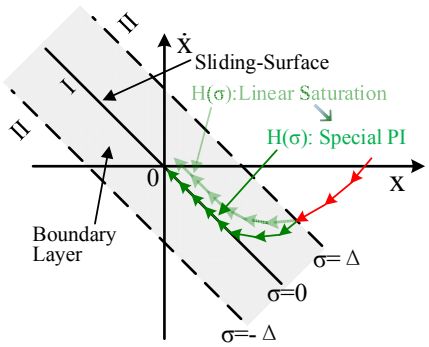

Fig. 9. Convergent trajectory of improved quasi-sliding mode method.

$$k_{id(q)}<\frac{k_{pd(q)}R}{L_{d(q)}}+\frac{k_{pd(q)}}{T_s} \tag{23}$$

After establishing the stability of the system, the error equation of the linear feedback system with the special PI regulator can then be similarly calculated as follows:

$$E(s)=\frac{-s(T_s s+1)(L_{d(q)}s+R)R(s)}{s(L_{d(q)}s+R)(T_s s+1)+k_{d(q)}(k_{pd(q)}s+k_{id(q)})} \tag{24}$$

where $R(s)$ is the input function. When $R(s)$ is the unit step function, the system's steady-state error can be obtained as Eq. (25).

$$e'_{ss}=\lim_{s\to 0}sE(s)=0 \tag{25}$$

Eq. (25) shows that the presented improved quasi-sliding mode method with a special PI regulator can eliminate a system's steady-state errors. Hence, the proposed method can increase observation accuracy and improve system performance.

The convergent trajectory of the improved quasi-sliding mode method is shown in Fig. 9. The light green curve is the convergent trajectory in region I when the control law is a linear saturation function. The dark green curve is the convergent trajectory in region I when the control law is the special PI regulator, which can stably move to the sliding surface. Thus far, the proposed control law can eliminate steady-state errors and ensure that the system moves to the sliding surface. Such capabilities prove that the convergence of the proposed improved quasi-sliding mode method is effective. Once the system moves to the sliding surface, the coupled EMF can be clearly observed. The current is then decoupled, and the back EMF is compensated for.

IV. PARAMETER DESIGN AND ROBUSTNESS ANALYSIS

A motor's parameter robustness is an important evaluation for the proposed method. The parameter design must be presented first prior to its discussion. In this section, the parameter design and robustness analysis of regions I and II are separately provided.

A. Parameter Design and Robustness Analysis in Region II

Only the SMO gains k_d and k_q must be designed in region II. The design rule of $k_{d(q)}$ should satisfy Eq. (16) and should be as small as possible.

For the robustness analysis in region II, Eq. (6) can be rewritten as follows:

$$\dot{\sigma} = A\sigma + Bu \tag{26}$$

$$\dot{\sigma} = \begin{bmatrix} \dot{\sigma}_d \\ \dot{\sigma}_q \end{bmatrix}, \sigma = \begin{bmatrix} \sigma_d \\ \sigma_q \end{bmatrix},$$

$$u = \begin{bmatrix} \dfrac{-k_d H(\sigma_d) - e_d}{L_d} \\ \dfrac{-k_q H(\sigma_q) - e_q}{L_q} \end{bmatrix}, A = \begin{bmatrix} -\dfrac{R}{L_d} & 0 \\ 0 & -\dfrac{R}{L_q} \end{bmatrix}, B = \begin{bmatrix} 1 & 0 \\ 0 & 1 \end{bmatrix}$$

If the system parameters change, then the error Eq. (26) changes to Eq. (27).

$$\dot{\sigma} = A\sigma + Bu + \Delta A\sigma \tag{27}$$

According to sliding mode theory, the necessary and sufficient condition for the sliding mode to be independent of the parameter change ΔA is

$$rank[B, \Delta A] = rank[B] \tag{28}$$

Then

$$\dot{\sigma} = A\sigma + B(u + \Delta\tilde{A}\sigma) \ , \ \Delta A = B\Delta\tilde{A} \tag{29}$$

Although u in Eq. (29) contains motor parameters L_d and L_q, the deviation of u is viewed as part of $\Delta\tilde{A}\sigma$ when L_d and L_q change. Therefore, the deviation caused by parameter variations can be compensated for by the discontinuous control law u; the same is true for the traditional SMO [34]. The unit matrix B satisfies Eq. (28); therefore, parameter variations do not influence the convergence in region II.

B. Parameter Design and Robustness Analysis in Region I

k_d, k_q and the parameters of the PI regulator must be designed in region I. According to Fig. 9, the system open-loop transfer function is obtained as Eq. (30).

$$G(s) = \frac{\dfrac{k_{d(\mathrm{q})}k_{pd(q)}}{L_{d(\mathrm{q})}T_s}(s + \dfrac{k_{id(q)}}{k_{pd(q)}})}{s(s + \dfrac{R}{L_{d(\mathrm{q})}})(s + \dfrac{1}{T_s})} \tag{30}$$

$k_{d(q)}$ should be selected as the same value as that in region II to avoid chattering when the system switches among the regions.

$$\frac{k_{id(q)}}{k_{pd(q)}} = \frac{R}{L_{d(\mathrm{q})}} \tag{31}$$

$$G'_B(s) = \frac{\dfrac{k_{d(\mathrm{q})}k_{pd(q)}}{L_{d(\mathrm{q})}T_s}}{s^2 + \dfrac{s}{T_s} + \dfrac{k_{d(\mathrm{q})}k_{pd(q)}}{L_{d(\mathrm{q})}T_s}} \tag{32}$$

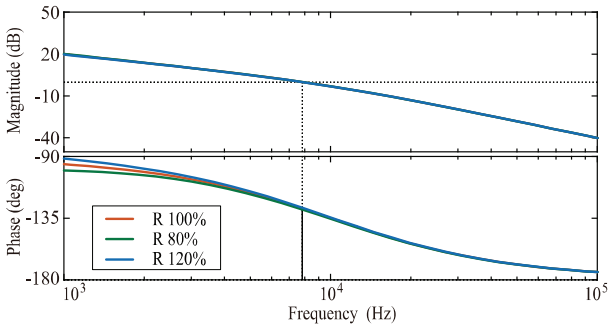

Fig. 10. Bode diagram of the SMO during resistance variation.

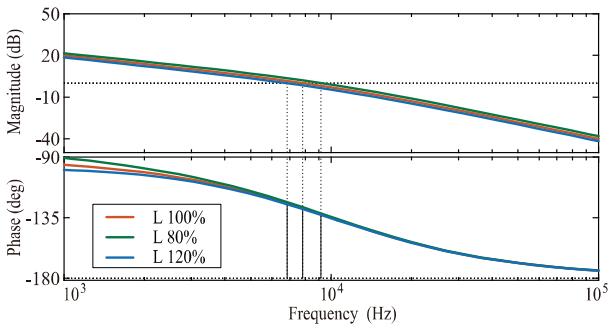

Fig. 11. Bode diagram of the SMO during inductance variation.

$k_{id(q)}$ and $k_{pd(q)}$ must satisfy Eq. (31) to transform Eq. (30) to a second-order system. The simplified function is shown in Eq. (32). Compared with the standard second-order system in Eq. (33), the Eq. (34) can be derived. $k_{pd(q)}$ can be calculated by Eq. (34), and $k_{id(q)}$ can be obtained by Eq. (31). Furthermore, $k_{id(q)}$ must satisfy Eq. (35); therefore, c in part C of Section III is positive, and the system is stable.

$$G_B(s) = \frac{\omega_n^2}{s^2 + 2\omega_n\xi s + \omega_n^2} \tag{33}$$

$$k_{pd(\mathrm{q})} = \frac{L_{d(\mathrm{q})}}{4k_{d(\mathrm{q})}T_s\xi^2} = \frac{L_{d(\mathrm{q})}T_s\omega_n^2}{k_{d(\mathrm{q})}} \tag{34}$$

$$k_{id(\mathrm{q})} < \frac{k_{pd(\mathrm{q})}R}{L_{d(q)}} + \frac{k_{pd(\mathrm{q})}}{T_s} \tag{35}$$

In addition, ω_n and ξ are called the undamped natural frequency and damping ratio of the standard second-order system, respectively. The overshoot decreases when ξ increases, and the response becomes fast when ω_n increases. $k_{pd(q)}$ and $k_{id(q)}$ are generally decided by ω_n and ξ. Notably, if ξ and ω_n are designed to be extremely large, then $k_{pd(q)}$ and $k_{id(q)}$ will not be correctly calculated, leading to system instability. The selection of ω_n and ξ should make a compromise between the response and overshoot to obtain a good performance.

With the aforementioned design strategy of parameters, the influence of resistance and inductance variation is analyzed. Fig. 10 is the Bode diagram of the open-loop feedback control system in region I when resistance variation occurs. For the simulation system, R is 2.88Ω, $L_{d(q)}$ is 6.4 mH, K_e is

48 *V/krpm*, ξ is 0.707, k_d is 59, k_{pd} is 1.08, and k_{id} is 488.1. The red curve is the Bode diagram with the original resistance R, the green curve is when the resistance R changes to 80%, and the blue one is that when resistance R changes to 120%. Based on the Bode diagram analysis, the amplitude and phase margins almost have no change when the motor parameter changes. Therefore, resistance R variation has less effect on the performance of the control system, and the system will still converge to the sliding surface.

Similarly, Fig. 11 is the Bode diagram of the open-loop feedback control system in region I when inductance variation occurs, and the same conclusion can be drawn to the inductance variation. Moreover, the permanent magnet flux linkage is not used in this method, and the current decoupling and the back EMF compensation will not be influenced by the permanent magnet flux linkage. Therefore, in region I, the system is robust to the parametric variations in steady state as verified in Section V.

V. Experimental Results

In this section, several experiments have been conducted to verify the validity of the proposed strategy. The experimental platform is shown in Fig. 12. Table III presents the parameters of the selected motor. The control algorithm is implemented on the MCU ADSP-CM408. The motor speed is measured by the photoelectrical-electricity encoder, and currents are measured by Hall sensor. The sampling period is 0.1 *ms*. These measured values are all sent to the upper monitor by a CAN-WIFI module.

Fig. 13 shows the block diagram of the control system. The detail of the improved quasi-SMO is shown in Fig. 2, and the equivalent control law is selected as Eq. (20). In Fig. 13, the velocity and current controllers are the PI regulators, and the improved quasi-SMO is used to estimate the coupling term in the $d(q)$-axis, which is shown in Eq. (2). The output of the PI current controller is combined with the output of the improved quasi-SMO to realize the current control. The current loop control cycle is 0.1 *ms*. According to the parameter design method introduced in Section IV, ξ is set as 0.707; therefore, the improved SMO parameters are obtained and listed as follows: for the q- and d-axes, the SMO gains k_q are 120 and 59, the control law's proportional coefficients k_{pq} are 0.53 and 1.08, and the integrating coefficients k_{iq} are 240 and 488.1, respectively. A small boundary layer width Δ will not be sufficient to eliminate chattering, whereas a large Δ will increase the adjustment time. Thus, the selection of Δ should make a compromise between chattering and adjustment time and is dependent on where the motor is applied. Δ is set as 0.5 in this study.

The first experiment compares the convergences of the common quasi-SMO discussed in part B of Section III and the improved quasi-SMO presented in part C of Section III. The current of the q-axis is selected as the reference object

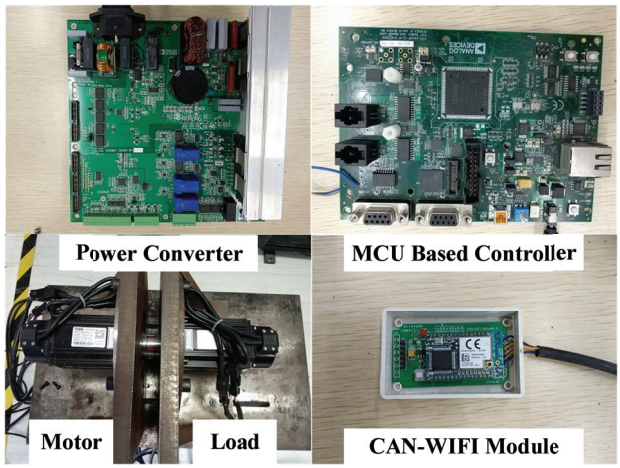

Fig. 12. Experimental platform.

TABLE III
Specification of Test PMSM

Rated power P_N	$0.75kW$
Rated voltage U_N	$220V$
Rated current I_N	$3.0A$
Rated speed n_N	$3000rpm$
Pole pairs n_p	4
Stator resistance R	2.88Ω
$d(q)$-axis inductance $L_{d(q)}$	$6.4mH$
Back EMF Constant K_e	$48V/krpm$

for comparison. Fig. 14(a) shows the observed current and feedback current response of the common quasi-SMO, which selects a linear saturation function as the equivalent control law. Static errors exist between the observed and feedback values in steady state. Therefore, the common quasi-SMO cannot converge to the sliding surface. Fig. 14(b) shows the observed current and feedback current response of the improved quasi-SMO, which selects a special PI regulator as the equivalent control law. The observed value can effectively converge to the feedback value. As indicated by the comparative experiment, the improved quasi-SMO is clearly effective for achieving convergence. Once the system is convergent, the coupled EMF of the $d(q)$-axis can be observed. Fig. 15 shows the observed results when the system is convergent. The red and black curves are the coupled EMFs of the q- and d-axes, respectively. Given that the first experiment verifies the validity of the quasi-SMO discussed in part C of Section III, in the next three experiments, all the abbreviations of the SMO will refer to those of the quasi-SMO, which selects a special PI regulator as the equivalent control law.

The second experiment compares the differences with or without the proposed decoupling control strategy in the control system when the motor is running with no load. For the system without the proposed decoupling control strategy, it is just the most basic motor control system that is shown in

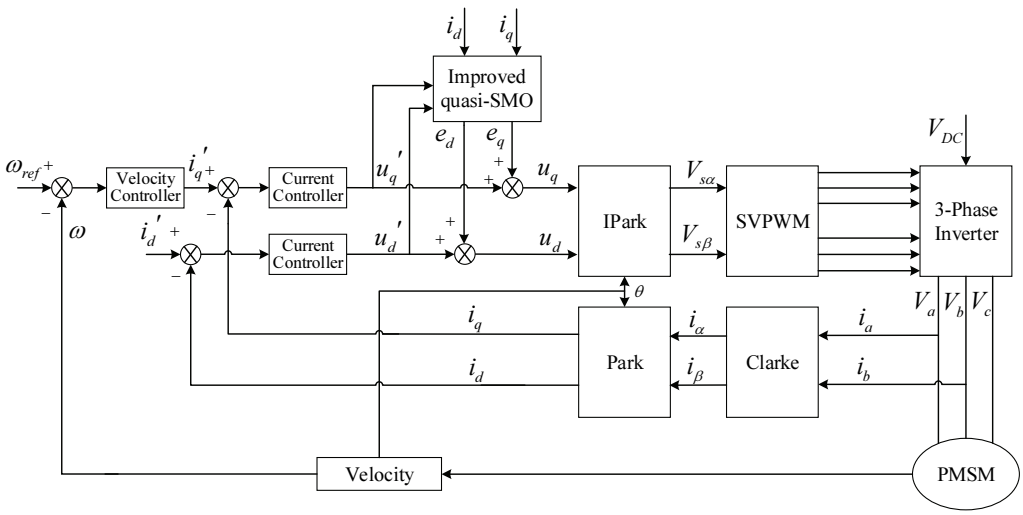

Fig. 13. Block diagram of overall system.

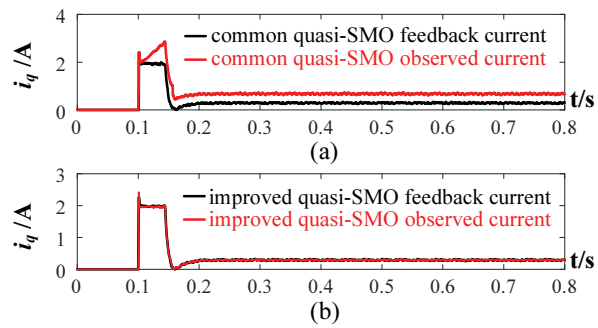

Fig. 14. Observed current and feedback current response: (a) Common quasi-SMO; (b) Improved quasi-SMO.

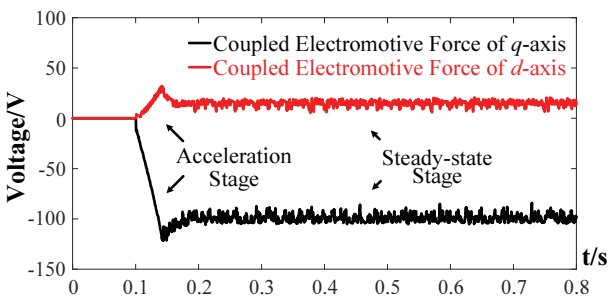

Fig. 15. Observed coupled EMF when the system is convergent.

Fig. 13 when the module improved quasi-SMO is removed, the current controller is a no decoupling PI regulator. The system parameters, such as the PI controllers, are similar in the contrast experiment to verify the validity of the proposed decoupling control strategy effectively. The instruction motor speed is a step signal from 0 *rpm* to 2000 *rpm* in the startup stage and suddenly increases from 2000 *rpm* to 2500 *rpm* at $t = 1\ s$. The instruction value of the *q*-axis current is 2 *A* in the accelerated stage because of the limited output of the PI controller speed. The instruction value of the *d*-axis current is zero.

Figs. 16 (a), (b), and (c) show the contrast of the current response of the *q*(*d*)-axis and the speed response curves with or without the proposed decoupling control strategy, respectively. For the control system without the SMO in the startup stage and in the stage with a sudden speed increase,

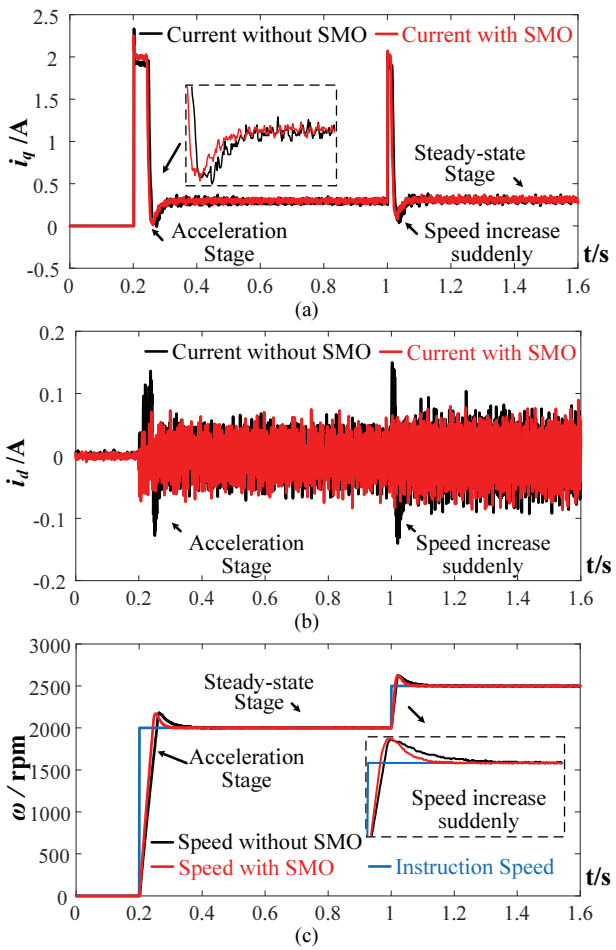

Fig. 16. Current and speed response with or without the proposed decoupling control strategy with no load: (a) Current in *q*-axis response; (b) Current in *d*-axis response; (c) Speed response.

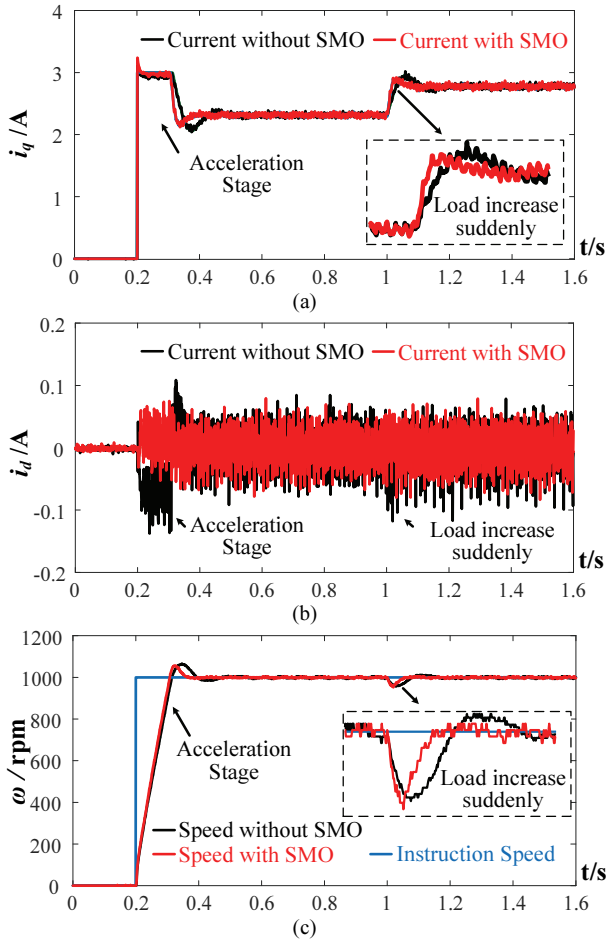

Fig. 17 Current and speed response with or without the proposed decoupling control strategy with load: (a) Current in *q*-axis response; (b) Current in *d*-axis response; (c) Speed response.

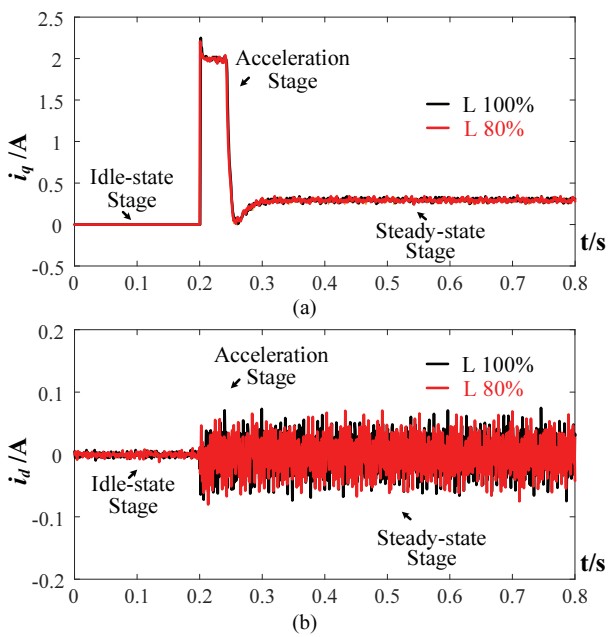

Fig. 18. Current response with the proposed strategy when the motor inductance changes: (a) Current in *q*-axis; (b) Current in *d*-axis.

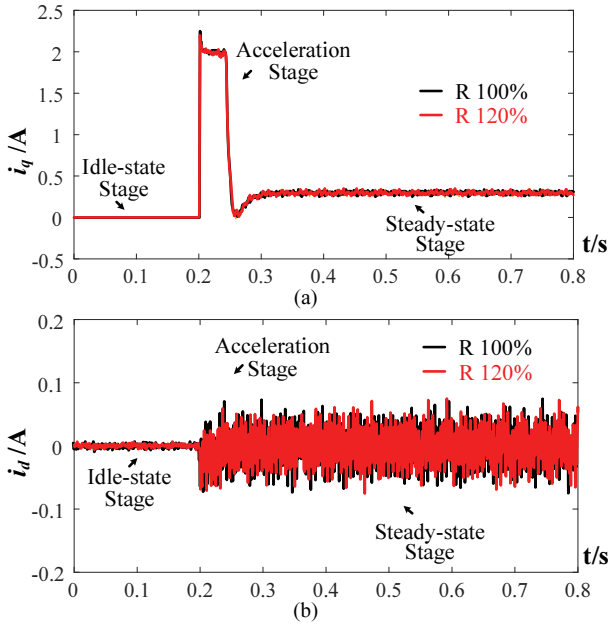

Fig. 19. Current response with the proposed strategy when the motor resistance changes: (a) Current in *q*-axis; (b) Current in *d*-axis.

the feedback current of the *q*-axis cannot rapidly follow the instruction value to the limited output due to the influence of the back EMF, as shown in Fig. 16(a). Meanwhile, the sudden change of the *q*-axis current exerts an influence on the *d*-axis current response because of the coupling between the two axes, as shown in the black curve of Fig. 16(b). When the proposed decoupling control strategy is utilized in the system, the *q*-axis current follows the instruction value well, as indicated by the red curve in Fig. 16. Moreover, the *d*-axis current no longer has the disturbance, as shown in the black curve in Fig. 16(b). According to the mathematical model of the PMSM in Fig. 1, the improvement of the *q*-axis current response depends mainly on the back EMF compensation, and the decrease in the *d*-axis current disturbance in the sudden speed change stage is completely dependent on the dynamic decoupling. The speed response is also improved due to the enhanced current response (Fig. 16(c)).

The third experiment compares the differences with or without the proposed decoupling control strategy when the motor is run with load. The instruction motor speed is 1000 rpm. The load torque is 0.96 *N.m* and suddenly increases to 1.2 *N.m* at $t = 1\ s$. The limited instruction value of the *q*-axis current is 3 *A*. The current and speed response curves are shown in Fig. 17.

Similar to the no-load experiment, the black curves correspond to the current and speed response in the control system without the SMO, and the red curves correspond to the proposed strategy. We compare the black and red curves in the startup and load changing stages. The results show that with the utilization of the proposed strategy, the current of the *q*-axis has a fast response, and the current of the *d*-axis no

longer has the disturbance, which is evident in the control system without the SMO. Thus, the second and third experiments show that the proposed strategy can achieve current dynamic decoupling and effectively compensate for the back EMF, ultimately leading to a satisfactory current response.

The fourth experiment compares the influences of the SMO on the motor parametric variations. In this experiment, the instruction motor speed is a step signal from 0 rpm to 2000 rpm. Fig. 18 shows the current response when the inductance changes to 80% of the original value. Fig. 19 shows the current response when the resistance changes to 120% of the original value. In Fig. 18, the black curve corresponds to the current response in which the motor inductance does not change when the proposed strategy is implemented. By contrast, the red curve corresponds to the current response in which the change of motor inductance is 80% when the proposed strategy is implemented. The current responses are clearly almost the same. Therefore, the proposed decoupling strategy is robust to inductance variations. The same conclusion can be drawn when the motor resistance changes according to Fig. 19. Therefore, the proposed decoupling strategy is evidently robust to parametric variations.

VI. CONCLUSIONS

A novel decoupling and compensation method based on an SMO is proposed. This method can reduce the negative influence from current dynamic coupling and back EMF in the vector control systems of PMSMs. The new method has a reduced dependence on motor models and is robust to disturbances from systems' parametric variations. Moreover, an improved SMO, which uses a special PI regulator other than a linear saturation function as the equivalent control law in the boundary layer of the sliding surface, is proposed to eliminate the estimated errors caused by the quasi-sliding mode. The stability and robustness of the proposed strategy are analyzed, and the experimental results confirm the validity and advantages of the decoupling and compensation method.

REFERENCES

[1] Q. Liu and K. Hameyer, "Torque ripple minimization for direct torque control of PMSM with modified FCSMPC," *IEEE Trans. Ind. Appl.*, Vol. 52, No. 6, pp.4855-4864, Nov./Dec. 2016.

[2] S. K. Kommuri, M. Defoort, H. R. Karimi, and K. C. Veluvolu," A robust observer-based sensor fault-tolerant control for PMSM in electric vehicles," *IEEE Trans. Ind. Electron*., Vol. 63, No. 12, pp.7671-7681, Dec. 2016.

[3] Q. Tang, A. Shen, X. Luo, and J. Xu, "PMSM sensorless control by injecting HF pulsating carrier signal into abc frame," *IEEE Trans. Power Electron*., Vol. 32, No. 5, pp. 3767-3776, May 2017.

[4] X. Luo, A. Shen, and R. Mao, "Double bi-quad filter with wide-band resonance suppression for servo systems," *J. Power Electron.*, Vol. 15, No. 5, pp. 1409-1420, Sep. 2015.

[5] X. Gan, C. Liu, and Y. Zuo, "Analysis and dynamic decoupling control schemes for PMSM current Loop," in *2016 IEEE International Conference on Aircraft Utility Systems (AUS),* pp. 570-574, 2016.

[6] Y. Mao, J. Yang, T. Wang, D. Yin, and Y. Chen, "High dynamic sensorless control for PMSMs based on decoupling adaptive observer," in *2016 IEEE Energy Conversion Congress and Exposition (ECCE),* pp. 1-8, 2016.

[7] F. Briz, M. W. Degner, and R. D. Lorenz, "Analysis and design of current regulators using complex vectors," *IEEE Trans. Ind. Appl*., Vol. 36, No. 3, pp. 817-825, May/Jun. 2000.

[8] X. Q. Tang, Y. C. Bai, and J. H. Chen, "Research on high-performance current decoupling control of PMSM," *Electric Drive*, Vol. 39, No. 10, pp. 18-22, 2009.

[9] R. Y. Deng, J. Tang, and Y. Xia, "Decoupling control of current loops for permanent magnet synchronous motor based on feedforward compensation," *Power Electronics*, 2013.

[10] W. Zhang, N. Zhang, and P. Chen, "Vector control system of induction motor based on feed-forward decoupling scheme," *Journal of Mechanical & Electrical Engineering*, 2013.

[11] H. Zhang and D. Z. Wang, "Vector control system of induction motor based on decoupling scheme," *Information Technology*, 2006.

[12] R. D. Lorenz and D. B. Lawson, "Performance of feedforward current regulators for field-oriented induction machine controllers," *IEEE Trans. Ind. Appl*., Vol. IA-23, No. 4, pp. 597-602, Jul. 1987.

[13] H. Zhu, X. Xiao and Y. Li, "PI type dynamic decoupling control scheme for PMSM high speed operation," in *2010 Twenty-Fifth Annual IEEE Applied Power Electronics Conference and Exposition (APEC),* pp. 1736-1739, 2010.

[14] J. Jung and K. Nam, "A dynamic decoupling control scheme for high-speed operation of induction motors," *IEEE Trans. Ind. Electron*., Vol. 46, No. 1, pp. 100-110, Feb. 1999.

[15] L. Harnefors and H. P. Nee, "Model-based current control of AC machines using the internal model control method," *IEEE Trans. Ind. Appl*., Vol. 34, No. 1, pp. 133-141, Jan./Feb. 1998.

[16] T. F. Chan, W. Wang, P. Borsje, Y. K. Wong, and S. L. Ho, "Sensorless permanent-magnet synchronous motor drive using a reduced-order rotor flux observer," *IET Electric Power Appl.*, Vol. 2, No. 2, pp. 88-98, Mar. 2008.

[17] A. Deng, J. Zou, Z. Shao, G. Huang, L. Shi, and J. Yang, "Internal and sliding mode current decoupling control of asynchronous motor," in *The 27th Chinese Control and Decision Conference (2015 CCDC),* pp. 3572-3577, 2015.

[18] P. O. Nyman and W. Sulkowski, "PMSM robust current control with adaptive tuning of axis decoupling," in *Industrial Electronics Society, 2003. IECON '03. The 29th Annual Conference of the IEEE*, pp. 2239-2244, 2003.

[19] H. Jin and J. Lee, "An RMRAC current regulator for permanent-magnet synchronous motor based on statistical model interpretation," *IEEE Trans. Ind. Electron*., Vol. 56, No. 1, pp. 169-177, Jan. 2009.

[20] N. Golea, A. Golea, and M. Kadjoudj, "Robust MRAC adaptive control of PMSM drive under general parameters uncertainties," in *2006 IEEE International Conference on Industrial Technology*, pp. 1533-1537, 2006.
[21] Y. Kim, K. S. Kim, and S. Kim, "A DOB based robust current control of permanent magnet synchronous motor," in *2015 15th International Conference on Control, Automation and Systems (ICCAS)*, pp. 301-306, 2015.
[22] J. W. Jung, Y. S. Choi, V. Q. Leu, and H. H. Choi, "Fuzzy PI-type current controllers for permanent magnet synchronous motors," *IET Electric Power Appl*., Vol. 5, No. 1, pp. 143-152, Jan. 2011.
[23] A. Massoum, E. M. Chiali, S. Massoum, A. Attou, and A. Meroufel, "Neuro-fuzzy control of an input output linearization of a permanent magnet synchronous machine fed by a three levels inverter," in *4th International Conference on Power Engineering, Energy and Electrical Drives*, pp. 92-96, 2013.
[24] M. Cheng, Q. Sun, and E. Zhou, "New self-tuning fuzzy PI control of a novel doubly salient permanent-magnet motor drive," *IEEE Trans. Ind. Electron*., Vol. 53, No. 3, pp. 814-821, Jun. 2006.
[25] R.-J. Wai and K.-M. Lin, "Robust decoupled control of direct field-oriented induction motor drive," *IEEE Trans. Ind. Electron*., Vol. 52, No. 3, pp. 837-854, Jun. 2005.
[26] M. Comanescu, L. Xu, and T. D. Batzel, "Decoupled current control of sensorless induction-motor drives by integral sliding mode," *IEEE Trans. Ind. Electron*., Vol. 55, No. 11, pp. 3836-3845, Nov 2008.
[27] M. Comanescu, "An induction-motor speed estimator based on integral sliding-mode current control," *IEEE Trans. Ind. Electron*., Vol. 56, No. 9, pp. 3414-3423, Sep. 2009.
[28] S.-H. Chang, P.-Y. Chen, Y.-H. Ting, and S.-W. Hung, "Robust current control-based sliding mode control with simple uncertainties estimation in permanent magnet synchronous motor drive systems," *IET Electric Power Appl.,* Vol. 4, No. 6, pp. 441-450, Jul. 2010.
[29] T. S. Gabbi, H. A. Gründling, and R. P. Vieira, "Sliding mode current control based on disturbance observer applied to permanent magnet synchronous motor," *Power Electronics Conference and, Southern Power Electronics Conference. IEEE*, pp. 1-6, 2015.
[30] H. Zhou, X. Wen, F. Zhao, and J. Zhang, "Decoupled current control of permanent magnet synchronous motors drives with sliding mode control strategy based on internal model," *Proceedings of the Csee*, Vol. 32, No. 5, pp. 91-99, May 2012.
[31] X. Liu, C. Zhang, K. Li, and Q. Zhang, "Robust current control-based generalized predictive control with sliding mode disturbance compensation for PMSM drives," *Isa Transactions*, Vol. 71, pp. 542-552, Nov. 2017.
[32] Z. Yi, C. Wenjie, and W. Haifeng, "Permanent magnet synchronous motor vector control based on weighted integral gain of sliding mode variable structure," *Open Automation & Control Systems Journal*, Vol. 7, No. 1, pp. 323-330, Apr. 2015.
[33] L. Qi, Y. Z. Yang, X. Bai, H. B. Shi, and W. L. Liu, "Study of permanent magnet synchronous motor current robust control based on adaptive fast terminal sliding mode control," *Applied Mechanics & Materials*, Vol. 365-366, pp. 887-896, 2013.
[34] V. I. Utkin and H. C. Chang, *Sliding Mode Control in Electro-Mechanical Systems*, CRC Press, pp. 881-886, 2002.

Hanlin Shen was born in Jiangsu Province, China, in 1990. He received his B.S. degree from the School of Electrical and Information Engineering, Wuhan Institute of Technology (WIT), Wuhan, China, in 2013. He is currently working toward his Ph.D. degree at the School of Automation, Huazhong University of Science and Technology (HUST). His current research interests include power electronics, high-performance PMSM drives, and motion control.

Xin Luo received his B.S. and M.S. degrees in Huazhong University of Science and Technology, Hubei, China, in 2007 and 2010, respectively. He is currently pursuing his Ph.D. degree in the same institution. His current research interests include PMSM drive systems and power conversion circuits.

Guilin Liang received his B.S. degree in Automation from the School of Automation, Huazhong University of Science and Technology, Wuhan, China, in 2015. He is currently working toward his M.S. degree in Control Science and Engineering in the same institution. His research interests include power electronics and motion control.

Anwen Shen received his B.S. and M.S. degrees from Zhejiang University, Zhejiang, China, in 1991 and 1994, respectively; and his Ph.D. degree in Electric Drives and Automation from the Department of Control Science and Engineering, Huazhong University of Science and Technology (HUST), Wuhan, China, in 1997. He is a Professor at the School of Automation in HUST. His current research interests include power electronics, electrical drives, and intelligent control.